

# Mechanism and Constitutive Model of a Continuum Robot for Head and Neck Cancer Radiotherapy

Olalekan Ogunmolu<sup>†</sup>, Xinmin Liu<sup>\*</sup>, and Rodney Wiersma<sup>\*</sup>

**Abstract**—We present a parallel soft robot mechanism and its model for the complete immobilization and motion correction of a patient’s deviation from target in head and neck cancer radiation therapy. Each soft robot within the mechanism contracts or expands in a radially symmetric fashion around the patient’s cranial region, deforming under the isochoric property of its incompressible material. Our design goal is to provide a real-time head and neck manipulation and motion correction that is needed during frameless and maskless cancer radiation therapy. We analyze the mechanical arrangement around the patient’s cranial region, derive the deformation model of these robots and then present simulation results. Our results show consistency of behavior in meeting AAPM positioning accuracy guidelines, with less than 1mm errors in test deformation cases for the soft robot using our proposed model. In a follow-up work, we provide the kinematics and dynamics of the mechanism with control results from test cases.

## I. INTRODUCTION

Radiation therapy (RT) is an increasingly effective cancer treatment modality, with more than half of all cancer patients managed with RT having higher survival rates [1]. To assure optimal treatment, it is important for the patient to remain in a stable pose on the treatment machine. The current clinical convention is to immobilize the patient with rigid metallic frames and masks in a process called frame- and mask-based immobilization (see Figure 1). However, these immobilization systems attenuate the radiation dose, lowering treatment quality, they do not offer real-time compensation due to the lack of closed-loop feedback, they cause patient discomfort and pain – especially when the scalp has to be opened in order to plant fiducials for patient tracking [2].

Systems such as the Cyberknife (see Figure 2), though ensuring complete non-invasive radiotherapy with implanted tiny gold fiducials to differentiate tumors from healthy tissues, are incapable of closed-loop, real-time head motion correction when the treatment beam is on as they are only capable of compensating motion with pre-calculated trajectories. Furthermore, they have limited effectiveness given their non-compliant parts that assume rigidity of the patient’s body.

Techniques devised for immobilization so far in clinics range from open-loop motion compensation systems, where the whole treatment is stopped whenever the patient deviates from target to closed-loop robot-in-the-loop compensation systems. Initial



Fig. 1: Mask/Frame Immobilization in Frame-based RT. [Image best visualized in colored print].

F&M RT research consisted of semi-rigid and soft immobilizing devices around the patient’s head and neck (H&N) region without a closed-loop feedback controller. These techniques were mostly evaluative studies meant to investigate the feasibility of non-rigid immobilization techniques in treatment planning [3]–[8]. Closed-loop approaches achieve a higher real-time positioning accuracy, in a technique called frameless and maskless (F&M) RT mostly for treatment planning case studies. These mechanisms utilize rigid parallel robots which provide better positioning accuracy owing to their inherent defenses against the large flexure torques and error magnification of open-loop kinematic chains.

These approach consists in using rigid electro-mechanical links connected at discrete joints to correct motions in controlled settings. Example implementations include the steel-cast assembled 4-DOF robot of [9], the HexaPOD parallel manipulator of [10], or the in-house fabricated Stewart-Gough platform of [11]. These rigid parallel robots that have emerged as a means of immobilizing patients come with the hazards of rigid manipulation systems collocated with human beings being that

- they share their dexterous workspace with the patients’



Fig. 2: The Cyberknife and 6-DOF robotic couch system. ©Accuray Inc. [Image best visualized in colored ink].

<sup>†</sup>Perelman School of Medicine, The University of Pennsylvania, Philadelphia, PA 19104, USA ogunmolo@pennmedicine.upenn.edu

\*Department of Radiation Oncology, The University of Chicago, Chicago, IL 60637, USA {xmliu, rwiersma}@uchicago.edu

Research reported in this publication was supported by National Cancer Institute of the National Institutes of Health under award number R01CA227124

body as well as tissues – a safety concern since these robots' rigid mechanical components exhibit almost no compliance,

- they lack compliance in their structures that minimize actuator “hard shocks” on the patients’ body, and
- they are incapable of providing sophisticated motion compensation that may be needed for respiratory and internal organs displacement that often cause deviation from target.

In these implementations, the attenuation of the ionizing radiation owing to interference with the mechanical robot components is often left unresolved. It is noteworthy that recent developments such as [12] proposes moving the robot underneath the patient’s body, away from the beam. However, it is not yet certain that this would fully resolve the radiation attenuation question. The human body is a natural system that needs to be manipulated with materials that can absorb much of the energy arising out of collisions, rather than rigid electro-mechanical components. To mitigate these issues, we proposed using inflatable air bladders (IABs) as motion compensators during F&M RT treatment [13]–[16]. Our IABs are continuum, compliant, and configurable (C3) soft robot (SoRo) actuators that provide therapeutic patient motion compensation during RT. These IABs inflate, deflate, extend or contract governed by their material moduli and stiffness, internal pressurization and incompressibility constraints when given a reference trajectory. To our knowledge, ours are the first to explore continuum compliant materials as actuation systems for cranial manipulation in robotic radiotherapy.

Here, we analyze and test the constitutive model of our new class of IABs. The rest of this paper is structured as follows: in § II, we present the overall continuum, compliant kinematic mechanism and analyze the deformation properties of the IAB in § III; we then provide and discuss simulation results in § IV. We conclude the paper in § V.

## II. MECHANISM DESCRIPTION

In previous works [13]–[15], we relied on a data-driven system identification approach to realize the overall system dynamics. Our resultant system model lumped the patient, treatment couch and IAB models. These models lacked high-fidelity that necessitates the memory-based adaptive control composite laws that we derived from inverse Lyapunov analysis. The approximation model of the ensuing neural-network controller is a feature that required extensive training to realize a suitable controller for our H&N immobilization. Our goal here is to realize constitutive models for the IAB chains and peripheral actuation mechanisms – capable of manipulating the patient’s H&N’s complete DOF motion in real-time during RT. This would enable us write closed-form expressions for the IAB chains’ complete kinematics.

### A. Motion-Compensation Setup

We now describe the mechanism of the complete immobilization system. We propose 3 IAB kinematic chains totaling 8 IABs around the patient’s H&N region as illustrated in the abstraction diagram of Figure 3. The IABs are made

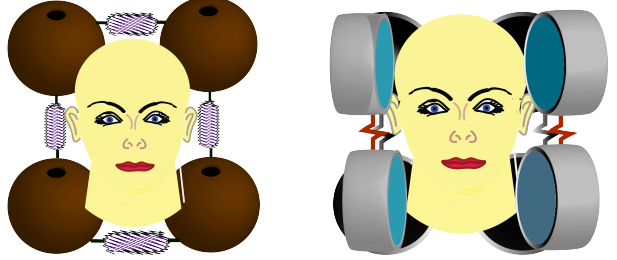


Fig. 3: An abstraction of the patient’s position correction mechanism. In the left image, there are four IABs that constitute the base kinematic chain. They lift the head along the Z-axis as well as provide pitch motion corrections. On the right, the side kinematic chains provide roll and yaw motion corrections. [Image best visualized in colored print].

out of silicone or rubber materials with a Poisson ration of approximately 0.5. They have two cavities. The internal cavity ensures the hollow IAB can hold the head in place during radiotherapy. The outer shell has an air enclosure that encapsulates the internal shell such that we can fulfill local volume preservation during deformation. This isochoric property and the incompressibility constraints of the IAB material walls is important in our mathematical derivations of the constitutive model of the compensating IAB mechanism. There exists two IAB chains to the each side of the patient’s H&N region. The side SoRo chains consist of two IABs, with each IAB making contact with the forehead and the chin/neck region at either symmetry of the patient’s head. Underneath the patient’s H&N is the third kinematic chain. This consists of four IABs, each positioned at four cardinal points beneath the patient’s H&N region. We would like the interconnection among the IABs to have a passive actuation such that when an IAB in a chain deforms, the rest of the IAB in the chain maintain contact with the patient’s H&N region. This is the purpose of the semi-plastic connectors attached between the IABs in each of the kinematic chains of Figure 3. Maintaining contact with the H&N region throughout deformation is a requirement for our the contact kinematics and H&N-IAB dynamics as described in [18]. The IABs change their configuration based on air that is conveyed into or out of their internal cavities when the sensed deviation of the patient from a target exceeds a setpoint or trajectory threshold . Each IAB is affixed to the H&N with radio-transparent semi-plastic connectors to prevent IAB free fall on the treatment table and around the patient’s head. Alternatively, as in our previous design [19], the patient can wear the IAB chains using the encapsulating shield as reproduced in Figure 4.

The degrees of freedom of the mechanism of Figure 3 can be determined using *Gruëbler-Kutzbach’s mobility condition*, wherein the number of degrees of freedom of a mechanism is given by (when the actuation results in a non-planar workspace configuration)

$$F = 6(N - g) + \sum_{i=1}^g f_i \quad (1)$$

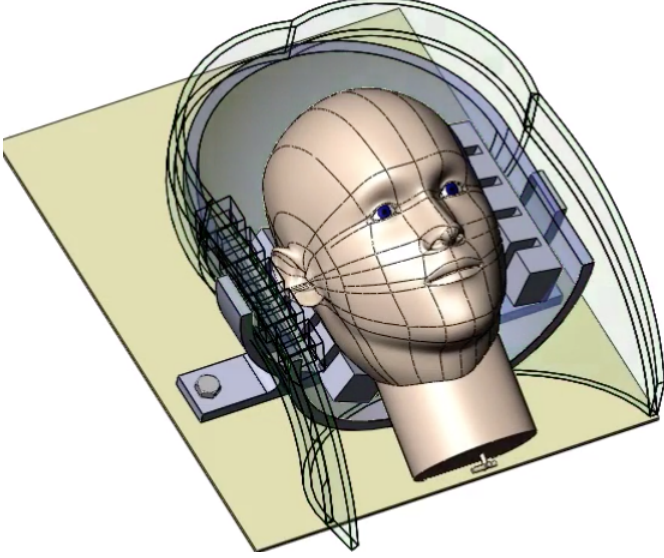


Fig. 4: Radio transparent wearable semi-plastic mask model that could hold IABs in place around the patient’s head and neck region. [Image best visualized in color print]. Unlike frame-based immobilization systems, the head can undergo

where  $N$  is the number of links in the mechanism,  $g$  is the number of joints,  $f_i$  is the total number of degrees of freedom for the  $i$ th joint. When the deformation of the mechanism results in a planar configuration, we have,

$$F = 3(N - g) + \sum_{i=1}^g f_i. \quad (2)$$

where through equations (1) and (2), the mechanism of Figure 3 have 16 DOFs since there are  $N = 8$  links,  $g = 8$  joints, and each joint has 2 DOFs .

### B. Finite Elastic Deformation Model

Realizing a closed-form model for the immobilization mechanism requires understanding the constituent dynamics of each IAB within the overall robot mechanism. In this sentiment, we propose a finite elastic deformation model [17], [20], [21], based on the deformation invariants of the stored energy function of each IAB. In what follows, we briefly describe our motivation for devising a finite elastic deformation model for the IAB mechanism. The constant curvature approach for parameterizing the deformation of continuum robots [22]–[24] has played significant role in the kinematic synthesis of deformable continuum models over the past two decades. Under this framework, the configuration space of a continuum module is parameterized by the curvature of an arc projected on the soft robot’s body, the arc’s length, and the angle subtended by a tangent along that arc. By abstracting an infinite dimensional structure to 3D, large portions of the manipulator dynamics are discarded under the assumption that the actuator design is symmetric and uniform in shape. This makes the constant curvature model overly simplified so that it often exhibits poor performance in position control [25]. While the Cosserat brothers’ beam theory has been relatively

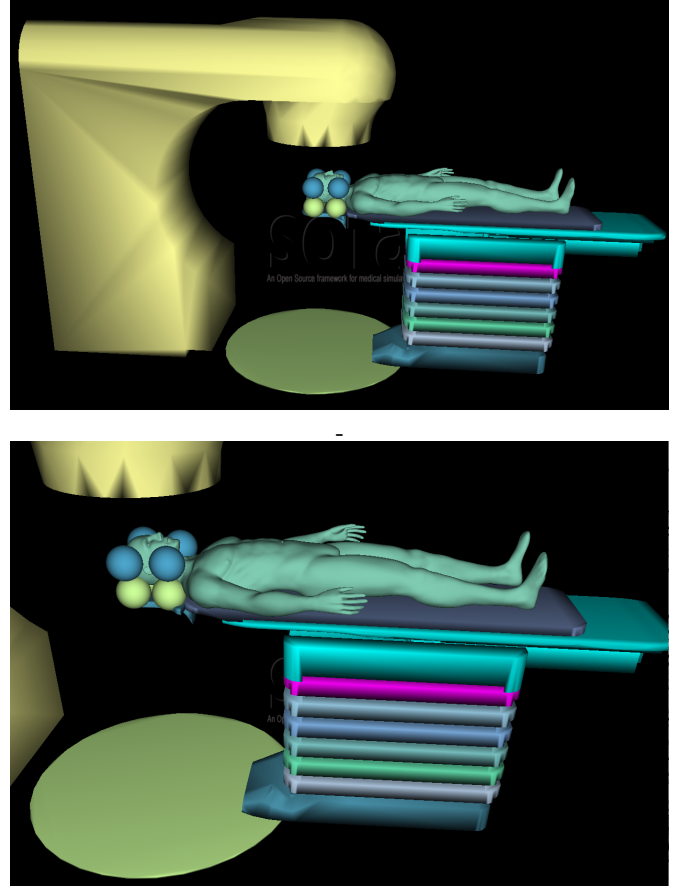


Fig. 5: System setup in the SOFA Framework Architecture. **Top:** Gantry, Turntable, Patient and IAB Chains around the patient’s H&N Region. **Bottom:** Close-up view of compensating IABs around patient’s H&N region with the patient lying in a supine position on the treatment couch. [Image best visualized in colored print].

successful in modeling soft continuum dynamics [26], [27], its complexity, and sensing cost does not justify the alternatives. Finite element modeling methods, while accurate, require heavy computation so that they are not very useful for our real-time control intentions. Therefore, we rigorously analyze the IABs’ deformation.

### Contributions:

- We propose an immobilization mechanism and construct a constitutive model for a new category of compliant, continuum and configurable (C3) IABs,
- We extend the principles of nonlinear elastic deformations [21] to isochoric strain deformations of these spherical IAB semi-rigid bodies, which are constructed out of materials with incompressible walls.
- We then analyze their deformation under stress, strain, internal pressurization, and an arbitrary hydrostatic pressure.

This kinematic model will then be used to develop the kinematics and Lagrangian dynamics of a multi-dof IAB SoRo motion correction mechanism as illustrated in Figure 5. Particularly, we analyze the deformation of a single semi-rigid robot body. In a follow-up paper [18], we address the

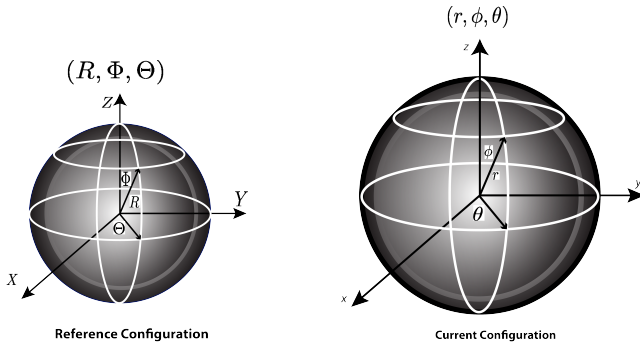


Fig. 6: Deformation in spherical polar coordinates.

kinematics, dynamics and control of the overall actuation system.

### III. DEFORMATION ANALYSIS OF AN IAB

In this section, we present the spherical polar coordinate representation of IAB deformation, derive the deformation gradient under assumptions of *isochoricity* and *incompressibility* of the IAB material skin. We then parameterize the configuration space of IAB kinematics based on a relationship between internal pressure, *Cauchy stress*, stored strain energy, and the radii of the IAB. The IABs are made out of rubber or elastomeric components which have the distinct property of incompressibility with a Poisson ratio of approximately 0.5 [28]. Our overarching assumption is that volume does not change locally during deformation at a configuration  $\mathbf{X}$  i.e. the deformation obeys *isochoricity*. Readers may refer to background reading materials in [17], [29] and [28].

#### A. Deformation Invariants

For a highly elastic, incompressible, and isotropic IAB under the action of applied forces, the deformation is governed by a stored energy function,  $W$ , which captures the physical properties of the material [30]. We choose two invariants,  $I_1$ , and  $I_2$ , described in terms of the principal extension ratios,  $\lambda_r, \lambda_\phi, \lambda_\theta$ , of the IAB's strain ellipsoids, defined as,

$$I_1 = \lambda_r^2 + \lambda_\phi^2 + \lambda_\theta^2, \quad \text{and} \quad I_2 = \lambda_r^{-2} + \lambda_\phi^{-2} + \lambda_\theta^{-2}. \quad (3)$$

Under the incompressibility assumptions of the IAB material body, we have that  $\lambda_r \lambda_\phi \lambda_\theta = 1$  [21]. In spherical coordinates, the change in polar/azimuth angles as well as radii in the reference and current configurations are as illustrated in Figure 6. Forces that produce deformations are derived using the strain energy-invariants relationship, i.e.,  $\frac{\partial W}{\partial I_1}$  and  $\frac{\partial W}{\partial I_2}$ .

#### B. Analysis of Strain Deformations

Suppose a particle on the IAB material surface in the reference configuration has coordinates  $(R, \Phi, \Theta)$  defined in spherical polar coordinates (see Figure 6), where  $R$  represents the radial distance of the particle from a fixed origin,  $\Theta$  is the azimuth angle on a reference plane through the origin and orthogonal to the polar angle,  $\Phi$ . Denote the internal

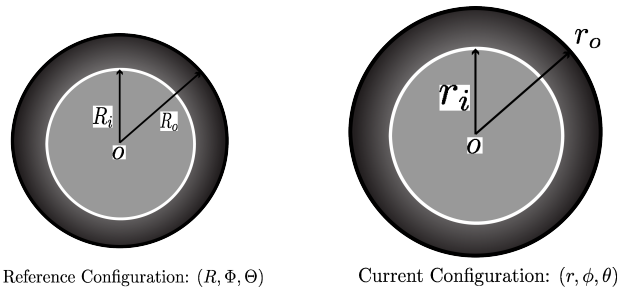


Fig. 7: Radii change under deformation.

and external radii as  $R_i$ , and  $R_o$  respectively. We define the following constraints,

$$R_i \leq R \leq R_o, \quad 0 \leq \Theta \leq 2\pi, \quad 0 \leq \Phi \leq \pi. \quad (4)$$

Now, suppose that the IAB undergoes deformation under the application of pressure on the internal IAB walls as depicted in Figure 7. Arbitrary points  $A$  and  $A'$  in the reference configuration become  $Q$  and  $Q'$  in the current configuration. Suppose that the vector that describes the *fiber* that connects points  $A$  and  $A'$  is  $a = a_R e_r + a_\Theta e_\Theta + a_\Phi e_\Phi$  where  $e_R, e_\Theta$ , and  $e_\Phi$  are respectively the basis vectors for polar directions  $R, \Theta$ , and  $\Phi$  such that its axial length stretches *uniformly* by an amount  $\lambda_z = \frac{r}{R}$ . We assume that there are internal constraints such that spherical symmetry is maintained during deformation of the incompressible IAB material shell. With the spherical symmetry of the IAB preserved, we have the following constraints in the current configuration

$$r_i \leq r \leq r_o, \quad 0 \leq \theta \leq 2\pi, \quad 0 \leq \phi \leq \pi. \quad (5)$$

The radial vectors  $\mathbf{R}$  and  $\mathbf{r}$  are given in spherical coordinates as,

$$\mathbf{R} = \begin{bmatrix} R \cos \Theta \sin \Phi \\ R \sin \Theta \sin \Phi \\ R \cos \Phi \end{bmatrix} \quad \text{and} \quad \mathbf{r} = \begin{bmatrix} r \cos \theta \sin \phi \\ r \sin \theta \sin \phi \\ r \cos \phi \end{bmatrix}. \quad (6)$$

The material volume  $\frac{4}{3}\pi(R^3 - R_i^3)$  contained between spherical shells of radii  $R$  and  $R_i$  remains constant throughout deformation, being equal in volume to  $\frac{4}{3}\pi(r^3 - r_i^3)$  so that

$$\frac{4}{3}\pi(R^3 - R_i^3) = \frac{4}{3}\pi(r^3 - r_i^3) \\ r^3 = R^3 + r_i^3 - R_i^3. \quad (7)$$

The homogeneous deformation between the two configurations imply that

$$r^3 = R^3 + r_i^3 - R_i^3, \quad \theta = \Theta, \quad \phi = \Phi, \quad (8)$$

where the coordinates obey the constraints of equations (4) and (5). Owing to the preservation of spherical symmetry, the *Lagrangian* and *Eulerian* axes coincide, with one axis aligned to the radial axis of the sphere and the other pair oriented arbitrarily normal to it so as to form a mutually orthogonal triad. The principal stretch along the azimuthal and zenith axes is therefore  $\lambda = \lambda_\theta = \lambda_\phi = r/R$ . Since for an isochoric deformation,  $\lambda_r \cdot \lambda_\theta \cdot \lambda_\phi = 1$ , it follows that the principal

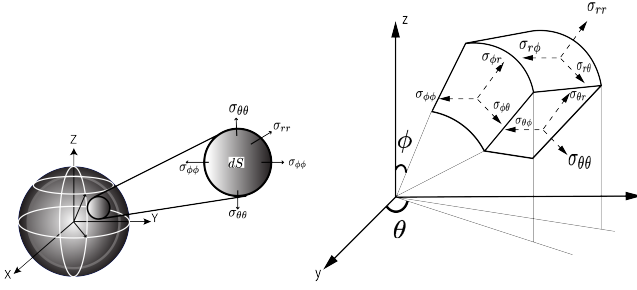


Fig. 8: Body stress distribution on continuum's differential surface,  $dS$ .

extension ratios are

$$\lambda_r = \frac{R^2}{r^2}; \lambda_\theta = \lambda_\phi = \frac{r}{R},$$

where  $\lambda_\theta, \lambda_\phi$  are the *azimuthal* and *polar principal stretch*. The Mooney-Rivlin strain energy for small deformations as a function of the strain invariants of (3), is,

$$W' = C_1(I_1 - 3) + C_2(I_2 - 3), \quad (9)$$

where  $C_1$  and  $C_2$  are appropriate choices for the IAB material moduli. The Mooney form (9) has been shown to be valid even for large elastic deformations, provided that the elastic materials exhibit incompressibility and are isotropic in their reference configurations [20]. For mathematical scaling purposes that will soon become apparent, we rewrite (9) as  $W = \frac{1}{2}W'$  so that

$$W = \frac{1}{2}C_1(I_1 - 3) + \frac{1}{2}C_2(I_2 - 3). \quad (10)$$

Note that equation (9) or (10) becomes the neo-Hookean strain energy relation when  $C_2 = 0$ . The deformation gradient  $\mathbf{F}$  in spherical polar coordinates, becomes

$$\begin{aligned} \mathbf{F} &= \lambda_r \mathbf{e}_r \otimes \mathbf{e}_R + \lambda_\phi \mathbf{e}_\phi \otimes \mathbf{e}_\Phi + \lambda_\theta \mathbf{e}_\theta \otimes \mathbf{e}_\Theta \\ &= \frac{R^2}{r^2} \mathbf{e}_r \otimes \mathbf{e}_R + \frac{r}{R} \mathbf{e}_\phi \otimes \mathbf{e}_\Phi + \frac{r}{R} \mathbf{e}_\theta \otimes \mathbf{e}_\Theta, \end{aligned} \quad (11)$$

where  $\otimes$  denotes the dyadics tensor product. The invariant equations, in polar coordinates, are therefore a function of the right Cauchy-Green and finger deformation tensors *i.e.*,

$$I_1 = \text{tr}(\mathbf{C}) = \frac{R^4}{r^4} + \frac{2r^2}{R^2}, \quad I_2 = \text{tr}(\mathbf{C}^{-1}) = \frac{r^4}{R^4} + \frac{2R^2}{r^2}. \quad (12a)$$

### C. Stress Laws and Constitutive Equations

We are concerned with the magnitudes of the differential stress on the IAB walls in spherical polar coordinates from a mechanical point of view. Since the IAB deforms at ambient temperature, we assume that thermodynamic properties such as temperature and entropy have little to no contribution. The IAB material stress response,  $\mathbf{G}$ , at any point on the IAB's boundary at time  $t$  determines the Cauchy stress,  $\sigma$ , as well as the history of the motion up to and at the time  $t$ . The constitutive relation for the nominal stress deformation for an

elastic IAB material is given by

$$\sigma = \mathbf{G}(\mathbf{F}) + q\mathbf{F} \frac{\partial \Lambda}{\partial \mathbf{F}}(\mathbf{F}), \quad (13)$$

where  $\mathbf{G}$  is a functional with respect to the configuration  $\chi_t$ ,  $q$  acts as a Lagrange multiplier, and  $\Lambda$  denotes the internal constraints of the IAB system. For an incompressible material, the indeterminate Lagrange multiplier becomes the hydrostatic pressure *i.e.*  $q = -p$  [29]. The incompressibility isotropic assumption of the IAB material properties imply that  $\Lambda \equiv \det \mathbf{F} - 1$ . As such, we find from (13) that

$$\begin{aligned} \sigma &= \mathbf{G}(\mathbf{F}) - p\mathbf{F}\text{adj}^T(\mathbf{F}) \\ &= \mathbf{G}(\mathbf{F}) - p\mathbf{F}\mathbf{F}^{-T}\det(\mathbf{F}) \\ &= \mathbf{G}(\mathbf{F}) - p\mathbf{I} \end{aligned} \quad (14)$$

where the last part of the equation follows from the isochoric assumption *i.e.*,  $\det(\mathbf{F}) = 1$ . In terms of the stored strain energy, we can rewrite (14) as

$$\sigma = \begin{bmatrix} \sigma_{rr} & \sigma_{r\phi} & \sigma_{r\theta} \\ \sigma_{\phi r} & \sigma_{\phi\phi} & \sigma_{\phi\theta} \\ \sigma_{\theta r} & \sigma_{\theta\phi} & \sigma_{\theta\theta} \end{bmatrix} = \frac{\partial W}{\partial \mathbf{F}} \mathbf{F}^T - p\mathbf{I}, \quad (15)$$

where  $\mathbf{I}$  is the identity tensor and  $p$  represents an arbitrary hydrostatic pressure. A visualization of the component stresses of (15) on the walls of the IAB material is illustrated in Figure 8. It follows that

$$\begin{aligned} \sigma &= \frac{\partial W}{\partial \mathbf{I}_1} \cdot \frac{\partial \mathbf{I}_1}{\partial \mathbf{F}} \mathbf{F}^T + \frac{\partial W}{\partial \mathbf{I}_2} \cdot \frac{\partial \mathbf{I}_2}{\partial \mathbf{F}} \mathbf{F}^T - p\mathbf{I} \\ &= \frac{1}{2}C_1 \frac{\partial \mathbf{I}_1}{\partial \mathbf{F}} \mathbf{F}^T + \frac{1}{2}C_2 \frac{\partial \mathbf{I}_2}{\partial \mathbf{F}} \mathbf{F}^T - p\mathbf{I} \\ &= \frac{1}{2}C_1 \frac{\partial \text{tr}(\mathbf{FF}^T)}{\partial \mathbf{F}} \mathbf{F}^T + \frac{1}{2}C_2 \frac{\partial \text{tr}([\mathbf{F}^T \mathbf{F}]^{-1})}{\partial \mathbf{F}} \mathbf{F}^T - p\mathbf{I} \\ &= C_1 \mathbf{FF}^T - C_2 (\mathbf{F}^T \mathbf{F})^{-2T} - p\mathbf{I} \\ &= C_1 \mathbf{B} - C_2 \mathbf{C}^{-2} - p\mathbf{I} \end{aligned} \quad (16)$$

where,  $\mathbf{C} = \mathbf{F}^T \mathbf{F}$  and  $\mathbf{B} = \mathbf{FF}^T$ . Thus, the constitutive law that governs the Cauchy stress tensor is

$$\sigma = C_1 \mathbf{B} - C_2 \mathbf{C}^{-2} - p\mathbf{I}. \quad (17)$$

It follows that the normal stresses are

$$\sigma_{rr} = -p + C_1 \frac{R^4}{r^4} - C_2 \frac{r^4}{R^4} \quad (18a)$$

$$\sigma_{\theta\theta} = \sigma_{\phi\phi} = -p + C_1 \frac{r^2}{R^2} - C_2 \frac{R^2}{r^4}. \quad (18b)$$

### D. IAB Boundary Value Problem

Here, we analyze the stress and internal pressure equations of the IAB at equilibrium. Consider the IAB with boundary conditions given by,

$$\sigma_{rr}|_{R=R_o} = -P_{\text{atm}}, \quad \sigma_{rr}|_{R=R_i} = -P_{\text{atm}} - P \quad (19)$$

where  $P_{\text{atm}}$  is the atmospheric pressure and  $P > 0$  is the internal pressure exerted on the walls of the IAB above  $P_{\text{atm}}$  *i.e.*,  $P > P_{\text{atm}}$ . Suppose that the IAB stress components satisfy

hydrostatic equilibrium, the equilibrium equations for the body force  $\mathbf{b}$ 's physical component vectors,  $b_r, b_\theta, b_\phi$  are

$$\begin{aligned} -b_r &= \frac{1}{r^2} \frac{\partial r^2 \sigma_{rr}}{\partial r} + \frac{1}{r \sin \phi} \frac{\partial \sin \phi \sigma_{r\phi}}{\partial \phi} + \frac{1}{r \sin \phi} \frac{\partial \sigma_{r\theta}}{\partial \theta} \\ &\quad - \frac{1}{r} (\sigma_{\theta\theta} + \sigma_{\phi\phi}) \end{aligned} \quad (20a)$$

$$\begin{aligned} -b_\phi &= \frac{1}{r^3} \frac{\partial r^3 \sigma_{r\phi}}{\partial r} + \frac{1}{r \sin \phi} \frac{\partial \sin \phi \sigma_{\phi\phi}}{\partial \phi} + \frac{1}{r \sin \phi} \frac{\partial \sigma_{\theta\phi}}{\partial \theta} \\ &\quad - \frac{\cot \phi}{r} (\sigma_{\theta\theta}) \end{aligned} \quad (20b)$$

$$\begin{aligned} -b_\theta &= \frac{1}{r^3} \frac{\partial r^3 \sigma_{\theta r}}{\partial r} + \frac{1}{r \sin^2 \phi} \frac{\partial \sin^2 \phi \sigma_{\theta\phi}}{\partial \phi} + \frac{1}{r \sin \phi} \frac{\partial \sigma_{\theta\theta}}{\partial \theta} \end{aligned} \quad (20c)$$

(see [31]). From the equation of balance of linear momentum (*Cauchy's first law of motion*), we have that

$$\operatorname{div} \boldsymbol{\sigma}^T + \rho \mathbf{b} = \rho \dot{\mathbf{v}} \quad (21)$$

where  $\rho$  is the IAB body mass density,  $\operatorname{div}$  is the divergence operator, and  $\mathbf{v}(\mathbf{x}, t) = \dot{\chi}_t(\mathbf{X})$  is the velocity gradient. Owing to the incompressibility assumption, we remark in passing that the mass density is uniform throughout the body of the IAB material. When the IAB is at rest,  $\dot{\mathbf{v}}_t(\mathbf{x}) = 0 \forall \mathbf{x} \in \mathcal{B}$  such that equation (21) loses its dependence on time. The assumed regularity of the IAB in the reference configuration thus leads to the steady state conditions for Cauchy's first equation; the stress field  $\boldsymbol{\sigma}$  becomes *self-equilibrated* by virtue of the spatial divergence and the symmetric properties of the stress tensor, so that we have

$$\operatorname{div} \boldsymbol{\sigma} = 0, \quad (22)$$

Equation 22 is satisfied if the hydrostatic pressure  $p$  in (17) is independent of  $\theta$  and  $\phi$ . Therefore, we are left with (20a) so that we have

$$\frac{1}{r} \frac{\partial}{\partial r} (r^2 \sigma_{rr}) = (\sigma_{\theta\theta} + \sigma_{\phi\phi}). \quad (23)$$

Expanding, we find that

$$\begin{aligned} \frac{1}{r} \left[ r^2 \frac{\partial \sigma_{rr}}{\partial r} + \sigma_{rr} \frac{\partial(r^2)}{\partial r} \right] &= (\sigma_{\theta\theta} + \sigma_{\phi\phi}) \\ \frac{1}{r} \left[ r^2 \frac{\partial \sigma_{rr}}{\partial r} + 2r \sigma_{rr} \right] &= (\sigma_{\theta\theta} + \sigma_{\phi\phi}) \\ r \frac{\partial \sigma_{rr}}{\partial r} &= \sigma_{\theta\theta} + \sigma_{\phi\phi} - 2\sigma_{rr} \quad (24) \\ \frac{\partial \sigma_{rr}}{\partial r} &= \frac{1}{r} (\sigma_{\theta\theta} + \sigma_{\phi\phi} - 2\sigma_{rr}). \end{aligned}$$

Integrating the above equation in the variable  $r$ , taking  $\sigma_{rr}(r_o) = 0$ , and carrying out a change of variables from  $r$  to  $R$ , we find that

$$\begin{aligned} \sigma_{rr}(\delta) &= - \int_{\delta}^{r_o} \frac{1}{r} (\sigma_{\theta\theta} + \sigma_{\phi\phi} - 2\sigma_{rr}) dr, \quad r_i \leq \delta \leq r_o \\ &= - \int_{\Delta}^{R_o} \frac{1}{r} (\sigma_{\theta\theta} + \sigma_{\phi\phi} - 2\sigma_{rr}) \frac{dr}{dR} dR, \quad R_i \leq \Delta \leq R_o \end{aligned}$$

$$\begin{aligned} &= - \int_{\Delta}^{R_o} \frac{R^2}{r^2} (\sigma_{\theta\theta} + \sigma_{\phi\phi} - 2\sigma_{rr}) dR, \quad R_i \leq \Delta \leq R_o \\ &= - \int_{\Delta}^{R_o} \left[ 2C_1 \left( \frac{1}{r} - \frac{R^6}{r^7} \right) - 2C_2 \left( \frac{R^6}{r^7} - \frac{r}{R^2} \right) \right] dR. \end{aligned} \quad (25)$$

In the same vein, using the boundary condition of (19)|<sub>2</sub> and taking the ambient pressure  $P_{\text{atm}} = 0$ , we find that

$$\begin{aligned} P &= \int_{R_i}^{R_o} \frac{R^2}{r^2} (\sigma_{\theta\theta} + \sigma_{\phi\phi} - 2\sigma_{rr}) dR, \quad R_i \leq R \leq R_o \\ &= \int_{R_i}^{R_o} \frac{r^2}{R^2} \left[ 2C_1 \left( \frac{1}{r} - \frac{R^6}{r^7} \right) - 2C_2 \left( \frac{R^6}{r^7} - \frac{r}{R^2} \right) \right] dr \\ &\equiv \int_{r_i}^{r_o} \left[ 2C_1 \left( \frac{r^3}{R^4} - \frac{R^2}{r^3} \right) - 2C_2 \left( \frac{R^4}{r^5} - \frac{r^3}{R^4} \right) \right] dr \end{aligned} \quad (26)$$

where  $r_i \leq r \leq r_o$ . Equations (25) and (26) completely determine the deformation kinematics of the IAB material at rest. In [18], we relate the head and neck force to the contact forces on the IAB surface boundary using the component stress laws just derived.

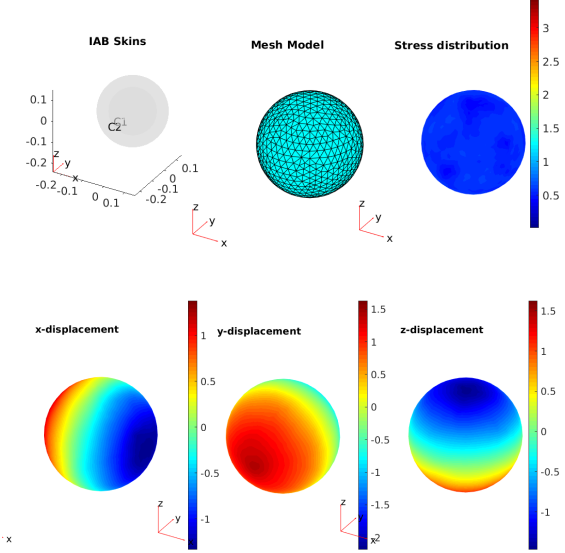
#### IV. SIMULATION AND RESULTS

For a Cauchy-Elastic IAB material we would like to find the pressure using (26) that deforms the IAB under the isochoric principle from the reference configuration radius,  $R_i$  to,  $r_i = R_i \pm \delta \text{ cm}$  in a current configuration for a given  $\delta$  with a corresponding change in  $r_o$  as given by  $r_o = \sqrt[3]{R_o^3 + r_i^3 - R_i^3}$ . The results shown in Figures 9, 10, 11 and 12 respectively represent the deformation behavior of the IAB material body under extension and compression respectively with different realistic material properties (stated in the tables beneath the figures). Note that all IAB radii dimensions are in  $\text{cm}$ , the pressure is given in  $\text{psi}$ ,  $C_1$  and  $C_2$  denote the IAB material moduli, and  $\nu$  is the Poisson ratio of the body in the tables.

For the given cases, the calculated pressure, and associated physical properties of the IAB are as given in the tables beneath the figure. To simulate the IAB body material, we apply a triangular mesh to the rigid IAB model using finite element modeling. We then compute the pressure that is required to uniformly expand the IAB from a reference to a current configuration (given by the values of  $R_o$  and  $r_o$  in the tables). The computed mesh model is shown in the top middle of the figures while the stress distribution after the application of the calculated pressure is shown in the upper-right corner of the figures. We choose a Poisson ratio of  $0.45 - 0.5$  to model the incompressibility material properties of the IABs.

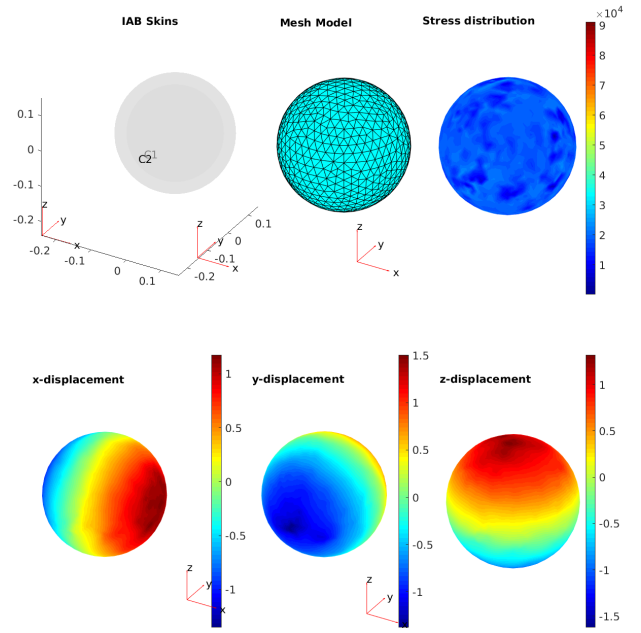
In the compression case of Figure 9, our goal was to uniformly expand the IAB from an outer radius of 15cm to 16cm in the current configuration. Notice a uniform expansion of 1.6cm along the three Cartesian axes of the spherical IAB in the lower charts of Figure 9. The deformation is a consequence of (26). We notice a similar consistency in Figure 10 with a required expansion of 3.21cm. The IAB extends by  $\sim 3.18\text{cm}$  along all three axes – exhibiting a positioning error of 0.3mm.

In the deformation cases of Figures 11 and 12, we present a uniform contraction of representative volumes of the isotropic and incompressible IAB under the application of the derived



$C_1$	$C_2$	$R_i$	$r_i$	$R_o$	$r_o$	$P$	$\nu$
$1.1e4$	$2.2e4$	10	13	15	16.60	14.552	0.45

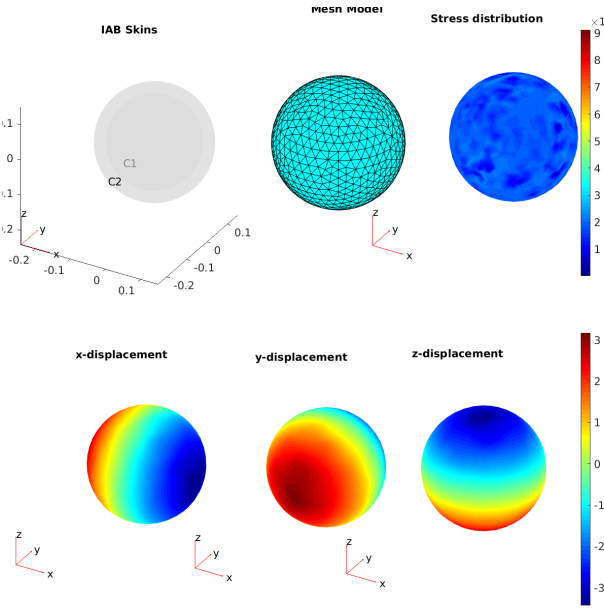
Fig. 9: IAB Expansion I (Charts best visualized in colored print).



$C_1$	$C_2$	$R_i$	$r_i$	$R_o$	$r_o$	$P$	$\nu$
$5e5$	$1.2e6$	12	10	15	13.83	-27.4	0.45

Fig. 11: IAB Compression I (Charts best visualized in colored print).

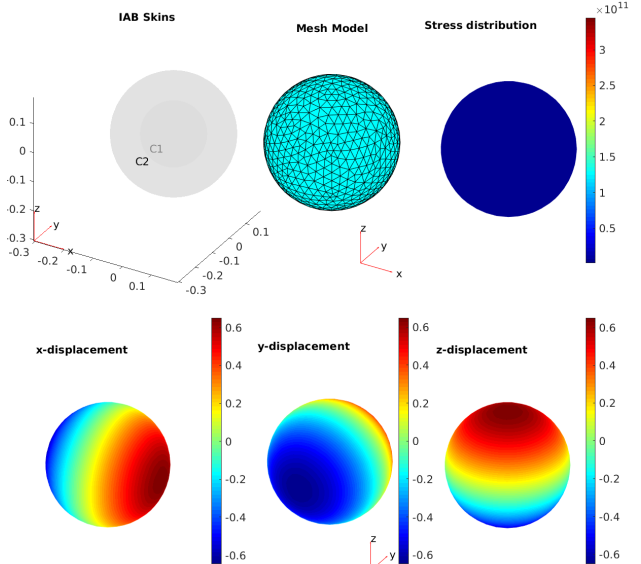
shrinking along the Cartesian axes of the IAB. For example, for a required shrink of 1.17cm from the reference configuration



$C_1$	$C_2$	$R_i$	$r_i$	$R_o$	$r_o$	$P$	$\nu$
$5e5$	$1e6$	7.5	12	10	13.21	14.5193	0.4995

Fig. 10: IAB Expansion II (Charts best visualized in colored print).

internal pressure for a desired radial shrink. The calculated negative pressures shown in the tables signify that air is being drawn out of the bladders. Again, we noticed an almost uniform Misses stress distribution on the IAB walls and an equal



$C_1$	$C_2$	$R_i$	$r_i$	$R_o$	$r_o$	$P$	$\nu$
$1.1e12$	$2.2e10$	10	8	19	18.54	-27.4	0.495

Fig. 12: IAB Compression II (Charts best visualized in colored print).

of [Figure 11](#), we notice a corresponding shrinkage along the desired directions by the required amount in the lower charts of the figure. For both figures of [Figure 11](#) and [Figure 12](#), notice that the deformation precision is well below the 2mm clinical accuracy recommended by the AAPM task group guidelines [32].

## V. CONCLUSION

We have presented the deformation analysis of a single inflatable air bladder using a constitutive model based on Truesdell's determinism from stress principle [33]. The deformation results presented in this work are well within the positioning accuracy requirements for head and neck immobilization in cancer RT as defined in the guidelines of the American Association for Physicists in Medicine Task Group 42 [32]. In a follow-up paper [18], we analyze the contact and deformation harmonics behavior of the IABs when they come in contact with the cranial region of the head. We then proceed to construct the kinematic model for full head and neck positioning control in real-time frameless and maskless radiation therapy. Future work would include physical IAB and IAB chains build as well as the implementation of the model described in this work on test patient cases.

## REFERENCES

- [1] L. Gaspar *et al.*, “Recursive Partitioning Analysis (rpa) of Prognostic Factors in three Radiation Therapy Oncology Group (rtog) Brain Metastases Trials,” *Int. J. Radiat. Oncol. Biol. Phys.*, vol. 37, p. 745751, 1997. [1](#)
- [2] T. Takakura, T. Mizowaki, M. Nakata, S. Yano, T. Fujimoto, Y. Miyabe, M. Nakamura, and M. Hiraoka, “The geometric accuracy of frameless stereotactic radiosurgery using a 6d robotic couch system,” *Physics in Medicine & Biology*, vol. 55, no. 1, p. 1, 2009. [1](#)
- [3] L. I. Cerviño, N. Detorie, M. Taylor, J. D. Lawson, T. Harry, K. T. Murphy, A. J. Mundt, S. B. Jiang, and T. A. Pawlicki, “Initial Clinical Experience with a Frameless and Maskless Stereotactic Radiosurgery Treatment,” *Practical Radiation Oncology*, vol. 2, no. 1, pp. 54–62, 2012. [1](#)
- [4] L. I. Cerviño, T. Pawlicki, J. D. Lawson, and S. B. Jiang, “Frame-less and mask-less cranial stereotactic radiosurgery: a feasibility study,” *Physics in medicine and biology*, vol. 55, no. 7, p. 1863, 2010. [1](#)
- [5] M. J. Murphy, R. Eidens, E. Vertatschitsch, and J. N. Wright, “The effect of transponder motion on the accuracy of the calypso electromagnetic localization system,” *International Journal of Radiation Oncology\* Biology\* Physics*, vol. 72, no. 1, pp. 295–299, 2008. [1](#)
- [6] A. Navarro-Martin, J. Cacicedo, O. Leaman, I. Sancho, E. García, V. Navarro, and F. Guedea, “Comparative analysis of thermoplastic masks versus vacuum cushions in stereotactic body radiotherapy,” *Radiation Oncology*, vol. 10, no. 1, p. 176, 2015. [1](#)
- [7] G. Li, A. Ballangrud, M. Chan, R. Ma, K. Beal, Y. Yamada, T. Chan, J. Lee, P. Parhar, J. Mechalakos, *et al.*, “Clinical Experience with two Frameless Stereotactic Radiosurgery (fsrs) Systems using Optical Surface Imaging for Motion Monitoring,” *Journal of Applied Clinical Medical Physics/American College of Medical Physics*, vol. 16, no. 4, p. 5416, 2015. [1](#)
- [8] A. Krauss, S. Nill, M. Tacke, and U. Oelfke, “Electromagnetic real-time tumor position monitoring and dynamic multileaf collimator tracking using a siemens 160 mlc: Geometric and dosimetric accuracy of an integrated system,” *International Journal of Radiation Oncology\* Biology\* Physics*, vol. 79, no. 2, pp. 579–587, 2011. [1](#)
- [9] X. Liu, A. H. Belcher, Z. Grelewicz, and R. D. Wiersma, “Robotic stage for head motion correction in stereotactic radiosurgery,” in *2015 American Control Conference (ACC)*. IEEE, 2015, pp. 5776–5781. [1](#)
- [10] C. Herrmann, L. Ma, and K. Schilling, “Model Predictive Control For Tumor Motion Compensation In Robot Assisted Radiotherapy,” *IFAC Proceedings Volumes*, vol. 44, no. 1, pp. 5968–5973, 2011. [1](#)
- [11] A. Belcher, “Patient Motion Management with 6-DOF Robotics for Frameless and Maskless Stereotactic Radiosurgery,” Ph.D. dissertation, The University of Chicago, 2017. [1](#)
- [12] X. Liu and R. D. Wiersma, “Optimization based trajectory planning for real-time 6DoF robotic patient motion compensation systems,” *PloS one*, vol. 14, no. 1, p. e0210385, 2019. [2](#)
- [13] O. P. Ogunmolu, X. Gu, S. Jiang, and N. R. Gans, “A real-time, soft robotic patient positioning system for maskless head-and-neck cancer radiotherapy: An initial investigation,” in *Automation Science and Engineering (CASE), 2015 IEEE International Conference on, Gothenburg, Sweden*. IEEE, 2015, pp. 1539–1545. [2](#)
- [14] O. P. Ogunmolu, X. Gu, S. Jiang, and N. R. Gans, “Vision-based control of a soft robot for maskless head and neck cancer radiotherapy,” in *Automation Science and Engineering (CASE), 2016 IEEE International Conference on, Fort Worth, Texas*. IEEE, 2016, pp. 180–187. [2](#)
- [15] O. Ogunmolu, A. Kulkarni, Y. Tadesse, X. Gu, S. Jiang, and N. Gans, “Soft-neuroadapt: A 3-dof neuro-adaptive patient pose correction system for frameless and maskless cancer radiotherapy,” in *IEEE/RSJ International Conference on Intelligent Robots and Systems (IROS), Vancouver, BC, CA*. IEEE, 2017, pp. 3661–3668. [2](#)
- [16] O. P. Ogunmolu, “A Multi-DOF Soft Robot Mechanism for Patient Motion Correction and Beam Orientation Selection in Cancer Radiation Therapy.” Ph.D. dissertation, The University of Texas at Dallas; The University of Texas Southwestern Medical Center, 2019. [2](#)
- [17] R. Ogden, *Non-linear Elastic Deformations*. Mineola, New York: Dover Publications Inc., 1997. [3, 4](#)
- [18] O. Ogunmolu, E. Pearson, X. Liu, and R. Wiersma, “Kinematics and Dynamics of a Continuum Robot Immobilization Mechanism for Cancer Radiotherapy,” *Submitted to IEEE Transactions on Robotics*, 2019., 2019. [Online]. Available: [scriptedonachip.com/downloads/Papers/ContinuumII.pdf](http://scriptedonachip.com/downloads/Papers/ContinuumII.pdf) [2, 3, 6, 8](#)
- [19] Y. Almubarak, A. Joshi, O. Ogunmolu, X. Gu, S. Jiang, N. Gans, and Y. Tadesse, “Design and development of soft robot for head and neck cancer radiotherapy,” in *Electroactive Polymer Actuators and Devices (EAPAD) XX*, vol. 10594. International Society for Optics and Photonics, 2018, p. 1059418. [2](#)
- [20] M. Mooney, “A theory of large elastic deformation,” *Journal of applied physics*, vol. 11, no. 9, pp. 582–592, 1940. [3, 5](#)
- [21] L. R. G. Treloar, *The physics of rubber elasticity*. Oxford University Press, USA, 1975. [3, 4](#)
- [22] M. W. Hannan and I. D. Walker, “Kinematics and the Implementation of an Elephant’s Trunk Manipulator and Other Continuum Style Robots,” *Journal of Robotic Systems*, vol. 20, no. 2, pp. 45–63, 2003. [3](#)
- [23] M. W. Hannan and I. D. Walker, “Novel Kinematics for Continuum Robots.” *Advances in Robot Kinematics*, 2000, pp. 227–238. [3](#)
- [24] B. A. Jones and I. D. Walker, “Kinematics for Multisection Continuum Robots.pdf”, vol. 22, no. 1, pp. 43–55, 2006. [3](#)
- [25] A. D. Kapadia, K. E. Fry, and I. D. Walker, “Empirical investigation of closed-loop control of extensible continuum manipulators,” in *2014 IEEE/RSJ International Conference on Intelligent Robots and Systems*. IEEE, 2014, pp. 329–335. [3](#)
- [26] F. Renda, M. Giorelli, M. Calisti, M. Cianchetti, and C. Laschi, “Dynamic model of a multibending soft robot arm driven by cables,” *IEEE Transactions on Robotics*, vol. 30, no. 5, pp. 1109–1122, 2014. [3](#)
- [27] D. Trivedi, A. Lotfi, and C. D. Rahn, “Geometrically Exact Models For Soft Robotic Manipulators,” *IEEE Transactions on Robotics*, vol. 24, no. 4, pp. 773–780, 2008. [3](#)
- [28] A. Gent, *Engineering with Rubber. How to Design Rubber Components*. Munich: Carl Hanser Verlag Publications, 2012. [4](#)
- [29] G. A. Holzapfel, T. C. Gasser, and R. W. Ogden, “A new constitutive framework for arterial wall mechanics and a comparative study of material models,” *Journal of elasticity and the physical science of solids*, vol. 61, no. 1-3, pp. 1–48, 2000. [4, 5](#)
- [30] R. S. Rivlin and D. W. Saunders, “Large Elastic Deformations of Isotropic Materials. VII. Experiments on the Deformation of Rubber,” *Philosophical Transactions of the Royal Society A: Mathematical, Physical and Engineering Sciences*, vol. 243, no. 865, pp. 251–288, 1950. [4](#)
- [31] Y.-c. Fung, P. Tong, and X. Chen, *Classical and computational solid mechanics*. World Scientific Publishing Company, 2001, vol. 2. [6](#)
- [32] T. H. Wagner, T. Yi, S. L. Meeks, F. J. Bova, B. L. Brechner, Y. Chen, J. M. Buatti, W. A. Friedman, K. D. Foote, and L. G. Bouchet, “A geometrically based method for automated radiosurgery planning,” *International Journal of Radiation Oncology\* Biology\* Physics*, vol. 48, no. 5, pp. 1599–1611, 2000. [8](#)
- [33] C. Truesdell and W. Noll, *The Non-Linear Field Theories of Mechanics*. Springer, 1965. [8](#)